






Cite this: DOI: 10.1039/d5cc04090f

Received 20th July 2025,
Accepted 8th September 2025

DOI: 10.1039/d5cc04090f

rsc.li/chemcomm

Tip-effect-induced water dissociation on dendritic Bi–Cu catalysts boosts electrochemical CO₂ reduction to formate

Yalan Guo, Pengxia Lei, Xiaoxiao Wei, Xian-Zhu Fu,  Shao-Qing Liu * and
Jing-Li Luo *

Electrochemical CO₂ reduction to formate is hindered by insufficient water dissociation kinetics at high reaction rates. Herein, the morphology-induced tip effects serve as an intrinsic strategy for enhancing water activation without external modifications, enabling efficient formate production with 94.9% faradaic efficiency and a partial current density of $-104.2 \text{ mA cm}^{-2}$.

Electrochemical CO₂ reduction (ECR) to formate offers a promising pathway for carbon neutrality and sustainable fuel production, addressing both CO₂ mitigation and chemical synthesis.^{1,2} However, achieving high-performance CO₂-to-formate conversion remains challenging due to the need for effective CO₂ activation and hydrogenation, processes that heavily depend on water dissociation to generate active hydrogen species (*H).^{3–7} Most catalysts, however, struggle with water dissociation under high reaction rates, limiting proton supply and slowing the overall process.⁸

To improve water dissociation, various co-catalysts or heteroatom dopants have been explored. Elements like sulfur and fluorine can enhance water dissociation due to their ability to modulate the electronic structure and create favorable adsorption sites for water molecules.^{9–11} Nevertheless, these dopants tend to leach over time, undermining catalyst stability and requiring frequent regeneration.¹² This issue emphasizes the need for stable, intrinsic water dissociation capabilities that do not rely on easily leachable modifiers.

Recent advances suggest that the tip effect, generated by sharp morphological features, can locally enhanced electric fields and influence ion distribution.^{13–15} Catalysts with dendritic or needle-like structures benefit from this effect, concentrating electric field lines at these tips and enhancing mass

transport. This results in the enrichment of cations, such as K⁺ ions commonly present in ECR electrolytes.¹⁶ These K⁺ ions at the catalyst surface undergo hydration, forming coordinated water molecules (K–H₂O) that possess distinctly different properties compared to hydrogen-bonded bulk water. These coordination water molecules exhibit weaker O–H bonds and enhanced dissociation tendency, making them more readily available for generating active *H species that facilitate the subsequent hydrogenation steps in ECR. This tip effect-induced water activation represents an intrinsic and stable approach to enhance water dissociation without requiring external modifications or dopants.

Building upon this understanding, we herein report the *in situ* construction of dendritic Bi–Cu alloy catalysts on copper foam substrates (denoted as Bi–Cu–D), which leverage the tip effect to achieve enhanced ECR-to-formate performance through improved water dissociation kinetics. Compared to their irregular particle-shaped counterparts (denoted as Bi–Cu–NPs), the dendritic Bi–Cu catalysts demonstrate superior formate selectivity and activity. The Bi–Cu–D catalyst achieves a high faradaic efficiency of formate (FE_{formate}) over 94.9% at -1.0 V vs. RHE and a partial current density (j_{formate}) of $-104.2 \text{ mA cm}^{-2}$ at -1.8 V vs. RHE . Through COMSOL simulations, we reveal that the dendritic morphology creates intensified interfacial electric fields that promote K⁺ ion enrichment. The accumulated K⁺ ions increase the local concentration of coordination water molecules (K–H₂O), which exhibit enhanced dissociation capability relative to hydrogen-bonded water, thereby facilitating *H generation for the protonation process. *In situ* attenuated total reflection surface-enhanced infrared absorption spectroscopy (ATR-SEIRAS) further confirms the elevated K–H₂O ratio on the Bi–Cu–D surface. This work demonstrates that morphology-induced tip effects can serve as an intrinsic strategy for water activation, offering a stable and modification-free approach to enhance ECR performance through rational interfacial engineering.

The detailed synthetic procedure for both Bi–Cu–D and Bi–Cu–NPs are provided in the Experimental section of the SI. As

Shenzhen Key Laboratory of Energy Electrocatalytic Materials, Guangdong Provincial Key Laboratory of New Energy Materials Service Safety, Guangdong Research Center for Interfacial Engineering of Functional Materials, College of Materials Science and Engineering, Shenzhen University, Shenzhen, 518060, P. R. China. E-mail: sq.liu@szu.edu.cn, jll@szu.edu.cn



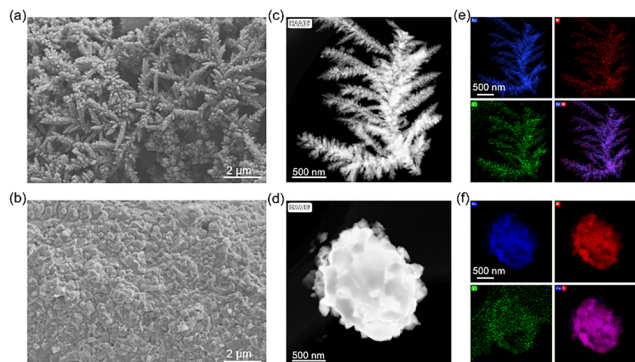


Fig. 1 SEM images of (a) Bi-Cu-D and (b) Bi-Cu-NPs, (c) Scanning transmission electron microscopy images of Bi-Cu-D and (d) Bi-Cu-NPs, along with the corresponding energy-dispersive X-ray spectroscopy elemental mapping shown in (e) and (f), respectively.

shown in the scanning electron microscopy (SEM) images (Fig. 1a and b and Fig. S1), Bi-Cu-D exhibits a distinct dendritic morphology characterized by numerous high-curvature branches, in sharp contrast to the compact, irregular particulate structure of Bi-Cu-NPs. This morphological difference is anticipated to influence the distribution of interfacial electric fields and consequently the catalytic behavior. To further elucidate the structural and compositional characteristics of the catalysts, scanning transmission electron microscopy (STEM) coupled with energy-dispersive X-ray spectroscopy (EDX) was employed. STEM images confirm that Bi-Cu-D possesses a well-defined dendritic crystalline structure, whereas Bi-Cu-NPs displays an agglomerated nanoparticulate morphology (Fig. 1c and d). Elemental mapping *via* EDX demonstrates a uniform spatial distribution of Cu, Bi, and O in both materials (Fig. 1e and f). The dendritic network of Bi-Cu-D offers a high surface area and abundant high-curvature features, which collectively enhance local electric fields and facilitate mass transport—critical factors for accelerating interfacial charge-transfer processes during CO₂ electroreduction.

X-ray diffraction (XRD) patterns (Fig. 2a) confirm the crystalline phases of both Bi-Cu-D and Bi-Cu-NPs, with peaks corresponding to cubic Cu (PDF #04-0836) and rhombohedral Bi (PDF #44-1246). High-resolution transmission electron microscopy (HRTEM, Fig. 2b) further corroborates the crystalline nature of Bi-Cu-D, revealing lattice fringes of 0.236 nm and 0.205 nm, which correspond to the (104) plane of Bi and the (111) plane of Cu, respectively, consistent with the XRD results. Surface chemical states were examined using X-ray photoelectron spectroscopy (XPS). The Bi 4f spectra show two distinct sets of doublets: peaks at 157.0 eV and 162.6 eV are attributed to metallic Bi⁰, while peaks at 158.8 eV and 164.3 eV correspond to oxidized Bi³⁺ species, likely resulting from air exposure during sample handling (Fig. 2c).¹⁷ The Cu 2p spectra exhibit dominant peaks at 932.5 eV and 952.3 eV, characteristic of Cu⁰/Cu⁺ (Fig. 2d), indicating that both catalysts predominantly retain metallic copper. Collectively, these structural and surface analyses confirm that Bi-Cu-D and Bi-Cu-NPs possess highly crystalline bimetallic frameworks with minimal surface oxidation, which are favorable for promoting durable and efficient CO₂ electroreduction.

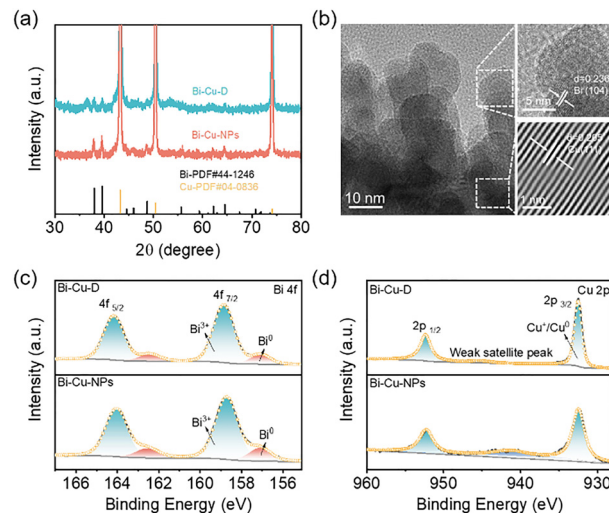


Fig. 2 Structural characterizations of Bi-Cu-D and Bi-Cu-NPs. (a) X-ray diffraction patterns of Bi-Cu-D and Bi-Cu-NPs, (b) high-resolution transmission electron microscopy image of Bi-Cu-D, (c) high-resolution Bi 4f XPS spectra of Bi-Cu-D and Bi-Cu-NPs, (d) high-resolution Cu 2p XPS spectra of Bi-Cu-D and Bi-Cu-NPs.

To evaluate the electrocatalytic performance of the synthesized catalysts, linear sweep voltammetry (LSV) was performed in a sealed H-cell using Bi-Cu-D and Bi-Cu-NPs as working electrodes. As shown in Fig. S2, both catalysts exhibited substantially higher cathodic currents in CO₂-saturated 0.5 M KHCO₃ compared to Ar-saturated conditions, confirming their inherent ECR activity. To further investigate product selectivity and catalytic efficiency, the FE_{formate} and j_{formate} were quantified over a range of applied potentials. Chronoamperometric electrolysis was conducted at potentials ranging from −0.8 to −1.8 V vs. RHE (Fig. S3a and b) to systematically evaluate the formate selectivity of Bi-Cu-D. As shown in Fig. 3a and b, Bi-Cu-D achieves outstanding ECR performance, maintaining a FE_{formate} above 90% between −1.0 and −1.6 V, with a peak FE_{formate} of 94.9% at −1.0 V. In comparison, the control catalyst Bi-Cu-NPs exhibits a lower maximum FE_{formate} of 92.1% under identical conditions. The corresponding j_{formate} values further underscore the performance advantage of Bi-Cu-D (Fig. 3c). At −1.8 V, Bi-Cu-D achieves a j_{formate} of −104.2 mA cm^{−2}, corresponding to a formate production rate as high as 1944.2 μmol h^{−1} cm^{−2}, significantly outperforming Bi-Cu-NPs, which only reaches 1689.6 μmol h^{−1} cm^{−2} under the same conditions (Fig. 3d). These results collectively highlight the superior catalytic efficiency of Bi-Cu-D for selective CO₂-to-formate conversion. To further clarify the origin of the activity difference, the electrochemically active surface area (ECSA) of catalysts was evaluated (Fig. S4a–c). The Bi-Cu-D catalyst exhibits a larger C_{dl} compared to Bi-Cu-NPs, confirming its higher electrochemically accessible surface area.

To assess the operational durability, long-term electrolysis was performed at −1.0 V using an H-cell. As presented in Fig. 3e, Bi-Cu-D maintains a stable current density of ~25 mA cm^{−2} over 24 h of continuous operation, with FE_{formate} consistently exceeding 90%, demonstrating excellent long-term



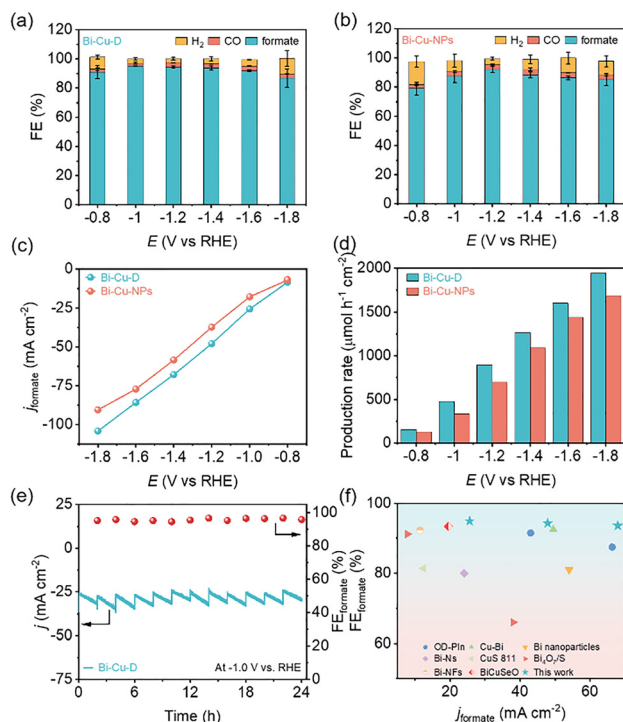


Fig. 3 Electrochemical CO₂RR to formate performance evaluation in H-cell. (a and b) Faradaic efficiency of electroreduction products generated by Bi-Cu-D and Bi-Cu-NPs, respectively, in CO₂-saturated 0.5 M KHCO₃ solution at different applied potentials. (c) j_{formate} of Bi-Cu-D and Bi-Cu-NPs, (d) Formate production rate of Bi-Cu-D and Bi-Cu-NPs, (e) Stability test of Bi-Cu-D at -1 V vs. RHE with electrolyte refreshed every 2 h, in CO₂-saturated 0.5 M KHCO₃ aqueous solution, (f) $\text{FE}_{\text{formate}}$ comparison of Bi-Cu-D with recently reported electrocatalysts.

stability. Moreover, Bi-Cu-D catalyst delivers a higher $\text{FE}_{\text{formate}}$ than most previously reported catalysts in H-cell (Fig. 3f and Table S1). Notably, Bi-Cu-D sustains high $\text{FE}_{\text{formate}}$ values across a broad current density range. In addition to enhanced formate production, Bi-Cu-D also exhibits a higher partial current density for hydrogen evolution compared to Bi-Cu-NPs (Fig. S5), suggesting a more active interfacial environment conducive to multiple proton-coupled pathways. This behavior is likely attributed to the tip-enhanced local electric field arising from its unique dendritic morphology, which promotes K-H₂O interfacial enrichment, facilitates water dissociation, and thereby accelerates the kinetics of ECR.

To gain deeper mechanistic insight into how structural modulation enhances ECR performance, we systematically investigated the role of interfacial microenvironment engineering. Finite element simulations reveal that the dendritic Bi-Cu-D catalyst, characterized by its high-curvature tip morphology, induces significantly intensified localized electric fields (Fig. S6). These enhanced fields promote surface enrichment of K⁺ ions (Fig. 4a). The synergistic interplay between interface regulation and cation accumulation accelerates water dissociation kinetics, thereby modulating the proton-coupled electron transfer (PCET) steps critical to ECR. To clarify the role of water activation in the reaction process, we evaluated the kinetic

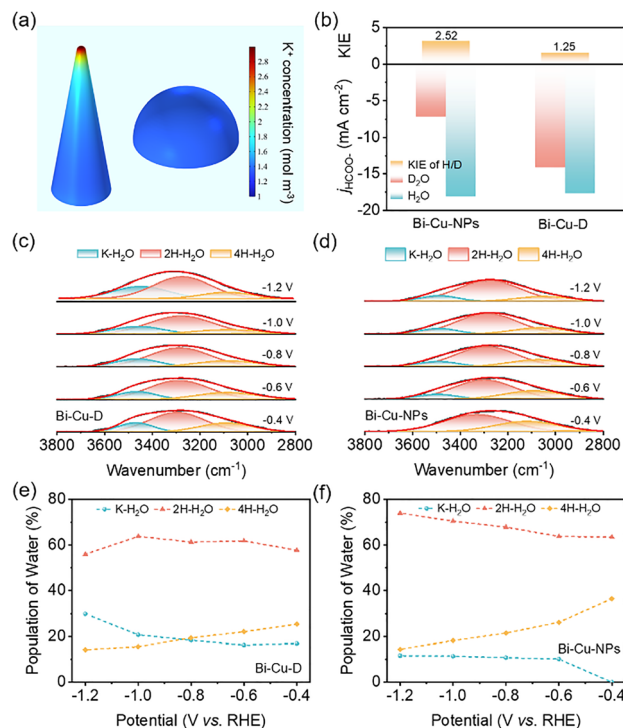


Fig. 4 (a) Simulated surface K⁺ concentration on dendritic and spherical particles, (b) Kinetic isotope effect results for the CO₂ reduction reaction on Bi-Cu-D and Bi-Cu-NPs at -0.85 V vs. RHE, *in situ* ATR-SEIRAS spectra under different applied potentials in CO₂-saturated 0.5 M KHCO₃ solution: (c) Gaussian fitting results of the O-H stretching vibration bands, where K-H₂O (high frequency), 2H-H₂O (mid frequency), and 4H-H₂O (low frequency) of Bi-Cu-D and (d) Bi-Cu-NPs, (e and f) Relative proportion of K-H₂O, 2H-H₂O and 4H-H₂O species on Bi-Cu-D and Bi-Cu-NPs under different applied potentials, respectively.

isotope effect (KIE) by comparing the catalytic behavior of Bi-Cu-D and Bi-Cu-NPs in H₂O- and D₂O-based electrolytes. The results revealed a KIE (H/D) value of 1.25 for formate production on Bi-Cu-D, indicative of a primary kinetic isotope effect.⁹ In contrast, the KIE value for Bi-Cu-NPs was only 2.52. This strongly supports that the Bi-Cu-D catalyst can effectively promote the water dissociation process, thereby accelerating ECR. To further validate this hypothesis, we employed *in situ* attenuated total reflectance surface-enhanced infrared absorption spectroscopy (ATR-SEIRAS) to monitor the O-H stretching vibrations of interfacial water. Deconvolution of spectra in the 2800–3800 cm⁻¹ region *via* Gaussian fitting identified three distinct components (Fig. 4c and d): 4-coordinated hydrogen-bonded water (4H-H₂O, low frequency), 2-coordinated hydrogen-bonded water (2H-H₂O, mid frequency), and K⁺-coordinated water (K-H₂O, high frequency).^{13,18} These spectral features reflect varied hydrogen-bonding environments and ion-solvent interactions, offering molecular-level insight into the enhanced selectivity and activity of Bi-Cu-D. The relative abundance of 4H-H₂O and 2H-H₂O is particularly relevant to the hydrogen evolution reaction (HER), as extended hydrogen-bonded networks tend to inhibit CO₂ activation. Notably, Bi-Cu-NPs exhibited stronger spectral intensities for both 4H-H₂O and 2H-H₂O (Fig. 4e and f), likely due to the presence of more



stable surface hydroxyl species, as confirmed by ATR-SEIRAS. These hydroxyl groups favor robust hydrogen-bonding networks that may suppress CO₂ adsorption and activation. Simultaneously, the K-H₂O species on Bi-Cu-NPs emerged only at potentials below -0.6 V, likely driven by electrostatic migration of K⁺ for charge compensation. In stark contrast, Bi-Cu-D exhibited significant K-H₂O signatures across a broader potential range, which we attribute to the combined effects of electrostatic migration and cation-specific adsorption, both enhanced by the intense interfacial fields created by the dendritic architecture. Moreover, the Stark tuning rate (*i.e.*, Stark slope) of K-H₂O vibrations on Bi-Cu-D was notably greater than that on Bi-Cu-NPs (Fig. S7), indicating higher sensitivity to interfacial electric fields and a thermodynamically more favorable K-H₂O formation process. This facilitated ion-solvent interaction is believed to enhance water dissociation and promote more efficient proton generation. *In situ* spectra further reveal stronger *OCHO signals at more positive potentials on Bi-Cu-D (Fig. S8),¹⁹ while EIS and Tafel analyses confirm its lower charge-transfer resistance and faster interfacial kinetics (Fig. S9 and S10). Altogether, these interfacial phenomena collectively account for the superior ECR kinetics and formate selectivity observed with the Bi-Cu-D catalyst.

In summary, we have developed a dendritic Bi-Cu electrocatalyst that leverages tip-enhanced localized electric fields to promote the surface enrichment of K⁺ ions, thereby facilitating water dissociation and significantly enhancing CO₂ electroreduction to formate. The catalyst achieves an impressive faradaic efficiency of 94.9% and a high partial current density of -104.2 mA cm⁻², surpassing its nanoparticulate counterpart and outperforming most previously reported catalysts operating in H-type cells. Mechanistic investigations reveal that the unique high-curvature morphology of Bi-Cu-D promotes the formation of K⁺-coordinated water species with weakened O-H bonds, thereby accelerating proton transfer kinetics. This work demonstrates a rational and effective strategy to engineer catalyst morphology and interfacial ionic environments for improved water activation and CO₂RR performance. Our findings offer valuable guidance for the design of next-generation electrocatalysts targeting efficient and selective CO₂-to-formate conversion.

This work was supported by the National Natural Science Foundation of China (22309116 and 22402124), the Shenzhen Science and Technology Program (No. ZDSYS20220527171401003, RCBS20231211090519029, KQTD20190929173914967). We thank Instrumental Analysis Center of Shenzhen University for the assistance with the Electron Microscope.

Conflicts of interest

There are no conflicts to declare.

Data availability

The data that support the findings of this study are provided within the manuscript or SI files. The SI file contains: Experimental procedures, Supplementary figures and tables referenced in the main text. See DOI: <https://doi.org/10.1039/d5cc04090f>.

Notes and references

- 1 N. Palanimuthu, M. R. Subramaniam, M. A. P. P. K. Sharma, V. Ramalingam, K. Peramaiah, S. Ramakrishnan, G. H. Gu, E. H. Yu and D. J. Yoo, *Small*, 2024, **20**, 2400913.
- 2 C. Zhang, X. Hao, J. Wang, X. Ding, Y. Zhong, Y. Jiang, M.-C. Wu, R. Long, W. Gong, C. Liang, W. Cai, J. Low and Y. Xiong, *Angew. Chem., Int. Ed.*, 2024, **63**, e202317628.
- 3 K. Wu, P. Yang, S. Fan, Y. Wu, J. Ma, L. Yang, H. Zhu, X. Ma, H. Gao, W. Chen, J. Jia and S. Ma, *J. Mater. Chem. A*, 2024, **12**, 33972–33983.
- 4 Y. Shi, Y. Wang, J. Yu, Y. Chen, C. Fang, D. Jiang, Q. Zhang, L. Gu, X. Yu, X. Li, H. Liu and W. Zhou, *Adv. Energy Mater.*, 2023, **13**, 2203506.
- 5 P.-X. Lei, S.-Q. Liu, Q.-R. Wen, J.-Y. Wu, S. Wu, X. Wei, R. Feng, X.-Z. Fu and J.-L. Luo, *Angew. Chem., Int. Ed.*, 2025, **64**, e202415726.
- 6 Z. Wei, J. Ding, Z. Wang, A. Wang, L. Zhang, Y. Liu, Y. Guo, X. Yang, Y. Zhai and B. Liu, *Angew. Chem., Int. Ed.*, 2024, **63**, e202402070.
- 7 Y. Cheng, Q. Li, M. I. B. Salaman, C. Wei, Q. Wang, X. Ma, B. Liu and A. B. Wong, *J. Am. Chem. Soc.*, 2025, **147**, 12438–12448.
- 8 N. Ye, K. Wang, Y. Tan, Z. Qian, H. Guo, C. Shang, Z. Lin, Q. Huang, Y. Liu, L. Li, Y. Gu, Y. Han, C. Zhou, M. Luo and S. Guo, *Nat. Synth.*, 2025, **4**, 799–807.
- 9 W. Ma, S. Xie, X.-G. Zhang, F. Sun, J. Kang, Z. Jiang, Q. Zhang, D.-Y. Wu and Y. Wang, *Nat. Commun.*, 2019, **10**, 892.
- 10 W. Ma, S. Xie, T. Liu, Q. Fan, J. Ye, F. Sun, Z. Jiang, Q. Zhang, J. Cheng and Y. Wang, *Nat. Catal.*, 2020, **3**, 478–487.
- 11 Y. Liu, Z. Wei, X. Su, X. Shi, L. Liu, T. Wang, X. Xu, M. Zhao, Y. Zhai, H. B. Yang and B. Liu, *Adv. Funct. Mater.*, 2025, **35**, 2403547.
- 12 M. Luo, Z. Wang, Y. C. Li, J. Li, F. Li, Y. Lum, D.-H. Nam, B. Chen, J. Wicks, A. Xu, T. Zhuang, W. R. Leow, X. Wang, C.-T. Dinh, Y. Wang, Y. Wang, D. Sinton and E. H. Sargent, *Nat. Commun.*, 2019, **10**, 5814.
- 13 Z. Wang, D. Liu, C. Xia, X. Shi, Y. Zhou, Q. Liu, J. Huang, H. Wu, D. Zhu, S. Zhang, J. Li, P. Deng, A. S. Vasenko, B. Y. Xia and X. Tian, *Nat. Commun.*, 2025, **16**, 1754.
- 14 J. Gu, S. Liu, W. Ni, W. Ren, S. Haussener and X. Hu, *Nat. Catal.*, 2022, **5**, 268–276.
- 15 Y. Li, J. Li, W. Ai, J. Chen, T. Lu, X. Liao, W. Wang, R. Huang, Z. Chen, J. Wu, F. Cheng and H. Wang, *Angew. Chem., Int. Ed.*, 2024, **63**, e202407772.
- 16 R. Yang, M. Wu, D. Huang, Y. Yang, Y. Liu, L. Zhang, F. Lai, B. You, J. Fang, T. Liu, Y. Liu and T. Zhai, *Energy Environ. Sci.*, 2024, **17**, 2897–2907.
- 17 Z. Li, B. Sun, D. Xiao, Z. Wang, Y. Liu, Z. Zheng, P. Wang, Y. Dai, H. Cheng and B. Huang, *Angew. Chem., Int. Ed.*, 2023, **62**, e202217569.
- 18 C.-J. Zou, Z.-Y. Du, W. Tang, Q. Liu, X.-B. Liu, J.-C. Dong, P.-P. Fang and J.-F. Li, *Adv. Mater.*, 2025, DOI: [10.1002/adma.202503010](https://doi.org/10.1002/adma.202503010).
- 19 S. Zhang, W. Ruan and J. Guan, *Adv. Energy Mater.*, 2025, **15**, 2404057.

